Mars Entry Simulation of Slotted Compression Ramp Probe

A project present to
The Faculty of the Department of Aerospace Engineering
San Jose State University

in partial fulfillment of the requirements for the degree
Master of Science in Aerospace Engineering

By

Anthony DiQuattro

December, 2017

approved by

Dr. Periklis Papadopoulos
Faculty Advisor

The Designated Project Advisor Approves the Thesis Titled

MARS ENTRY SIMULATION OF SLOTTED COMPRESSION RAMP PROBE

by

Anthony DiQuattro

APPROVED FOR THE DEPARTMENT OF AEROSPACE ENGINEERING

SAN JOSÉ STATE UNIVERSITY

December 2017

Dr. P. Papadopoulos Department of Aerospace Engineering Advisor

ABSTRACT

MARS ENTRY SIMULATION OF SLOTTED COMPRESSION RAMP PROBE

by Anthony DiQuattro

This report summarizes aerodynamic simulations and heating analysis performed on the Slotted Compression Ramp (SCRAMP) probe for Mars Entry for polar scientific missions.

TABLE OF CONTENTS

NOMENCLATURE

A	reference area
C_A	axial force coefficient
C_P	pressure coefficient
k	thermal conductivity
P	pressure
Pr	Prandtl number
Q	dynamic pressure
q	heat flux
Re	Reynolds number
T	temperature
V	velocity
Θ	body angle
ρ	density
τ	shear stress
$()_f$	forward reaction parameter
$()_{LE}$	leading edge parameter
$()_r$	reverse reaction parameter
$()_{TE}$	trailing edge parameter
$()_\infty$	free stream parameter

CHAPTER 1

INTRODUCTION

1.1 Background

There is a great scientific interest in exploring Mars for geological data to determine its current and past characteristics. The polar regions are of particular interest because they currently contain water-ice on their surface, which raises the possibility of conditions on Mars surface that support liquid water. Missions involving sending experiments to Mars are both costly and high risk, since only 7 of 14 payloads sent to conduct experiments on the surface functioned after landing successfully [1].

The SCRAMP probe geometry presents a unique opportunity for future experiments. Its geometry provides an atmospheric entry vehicle with an aerodynamic center aft of the center of gravity, it is passively stable. By eliminating active entry control systems such as attitude control thrusters, probability of mission failure is greatly decreased. The probe can be implemented initially as a Space Station sample return vehicle with potential for scalability as a planetary probe. Testing has been performed with this geometry in suborbital reentry experiments, but comprehensive aerodynamic simulations are required to validate the SCRAMP as a solution for Mars atmospheric entry [2].

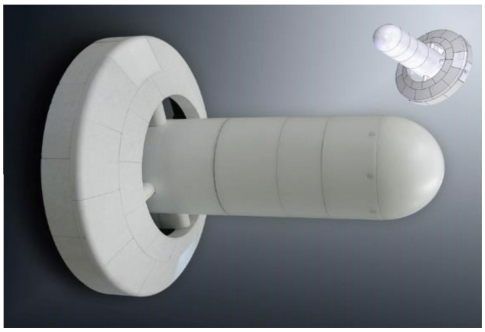

Figure 1.1 - Slotted Compression Ramp Probe.

A freestream flow Mach number of greater than 5 defines a hypersonic flow, which is significant due to phenomena in the shock region and boundary layer of an aerodynamic body. These high velocities experienced by vehicles entering an atmosphere create a strong upstream shockwave and alters the state of the fluid in its wake. The internal energy of the fluid in the free stream is overshadowed by the great kinetic energy of the free stream flow. Density of the flow around the body increases with the Mach number in the hypersonic regime, which forces the shock layer closer to the body [3].

The high density ratio across the shock wave in a hypersonic flow allows the mass of the fluid to be compressed into a smaller area, thus the thin shock wave [4]. This characteristic can create physical challenges when the shock layer begins interacting with the boundary layer.

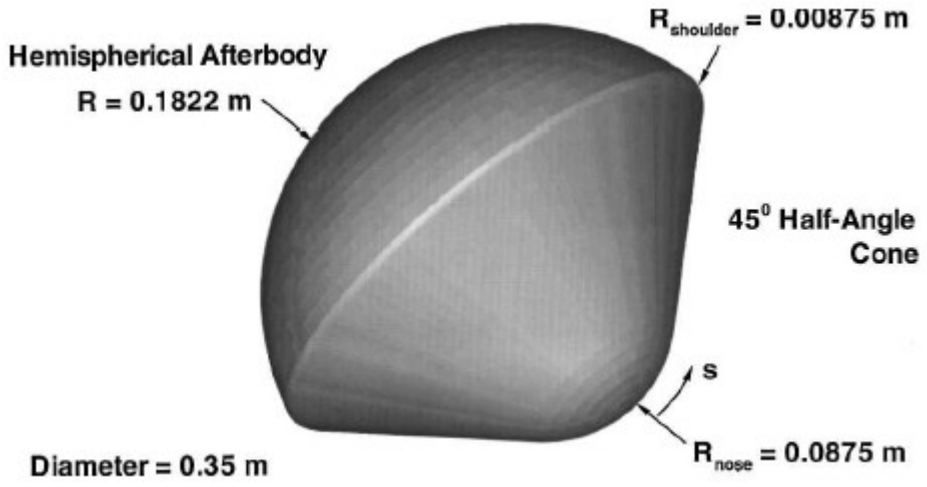

Figure 1.2 – Conventional sphere-cone geometry of DS-2 Mars probe [5].

1.2 Previous Work

The NASA Deep Space 2 mission included two small probes that landed on the Martian South Pole with the goal of demonstrating viability and collecting data on the properties of the

atmosphere and surface. Both the probes and the accompanying lander failed to transmit data after landing. The mission was developed and executed with limited time and funding, leading to engineering decisions to bypass testing and make educated assumptions on propulsion and control systems. This lack of testing resulted in an unknown cause of failure. Although entry data was not returned, this experiment provided a great deal of test data and theoretical analysis on Mars entry for small probes [5].

Similarly, the European Space Agency's Beagle 2 Mars lander mission failed to transmit data following entry and landing on Mars. In 2015, the NASA Mars Reconnaissance Orbiter captured and transmitted images of Beagle 2 on the planet surface. These images provided evidence that the lack of transmission was most likely due to failure of solar panel deployment, blocking the antenna. Confirmation of mission success up to landing shows that the aerodynamic entry modeling was sufficient [6].

The Stardust mission involved a probe spacecraft collecting dust samples from the trail of a comet as well as cosmic dust from within the solar system. The samples were collected in space and returned in a small reentry capsule for analysis. The probe entered at 12.9 km/s and encountered peak deceleration of 34 g, the fastest Earth entry of any scientific mission [7].

The Genesis mission profile, similar to Stardust, sent a probe to deep space for autonomous collection of solar wind particles and return to Earth for analysis. The probe reentered successfully but an error in integration prevented its parachute from deploying, causing damage and contaminating samples [8].

The SCRAMP body concept is a new approach to small probe atmospheric entry. By using passive stabilization methods, utilizing the shock-shock interactions and including multiple probes, probability of success can be increased.

To provide a solution for a given payload, the problem must be defined by the mission profile. This boils down to a given combination of drag, heating and stability requirements for the entry vehicle. The closest successful comparison missions to the potential ATROMOS payload by mass are the DS-2 probes. The Microprobe utilized a blunted cone heatshield fore body and hemispherical aft section to meet mission requirements. In part, the availability of previous flight data on the sphere-cone body from successful Venus and Jupiter probes was a major factor due to limited financial resources for research and testing. The entry vehicle design is flight proven to be dynamically stable if the center of gravity is set toward the cone fore body. Although the body is dynamically unstable when leading with the hemispherical side, the chance of the spacecraft reaching the unstable attitude can be minimized with spin stabilization. The hemispherical back shell also decreases dynamic instability in the transonic regime. The blunt cone fore body is selected for its drag and heating characteristics; the nose radius on the cone is a tradeoff between stability and heating characteristics. By increasing the nose radius, heating at the stagnation point is decreased but stability is lowered. The allowable heating is determined by material properties and volumetric constraints, and finally the entry vehicle can be sized for the desired ballistic coefficient [5].

By choosing a flight proven design, much of the previous research can be applied to the vehicle. We know that at hypersonic conditions above Mach 10, the bow shock has enough energy to disassociate CO_2 molecules. At the microprobe scale, gasses do not equilibrate across the thin shock layer. There is also existing wind tunnel data on sphere-cone probe geometries to predict supersonic aerodynamics, although there is less available in the transonic regime due to difficulties in testing and simulation.

The Mars Pathfinder entry vehicle also provided a useable atmospheric profile estimation from its entry, descent and landing data [10]. A study of wake flow about the Mars Pathfinder entry vehicle determined that accounting for ablation reduced fore body heating by 40-50%, whereas ablation effects on the aft body were nearly identical in ablating non ablating models [11]. A study in uncertainty analysis shows that in chemically reacting hypersonic flow simulations, surface heat flux is the greatest uncertainty. The biggest factor in heat flux uncertainty is variation in gas density, which greatly varies thermal properties at the entry vehicle shoulder and stagnation point [12].

Although NASA typically follows a "test as you fly" methodology for developing flight hardware, this sometimes isn't the case for reentry vehicles. Full scale flight condition thermal protection system testing is rarely performed due to cost, scheduling and limited facility resources. NASA Ames Research Center has developed a small probe platform named SPRITE (Small Probe Re-entry Investigation of TPS Engineering) for which there is published test data [13]. This serves as a baseline and comparison for a potential SCRAMP probe.

A series of small models were tested in an arc-jet. The objective of the study was to determine feasibility of full scale arc jet testing, perform in situ measurements and use software such as DPLR, FIAT and MARC to predict aerothermal flow properties and ablation effects of the vehicle. There were a few non ideal design compromises in the study. The first was modification of the vehicle geometry in removing the hemispherical back shell from the body for the model to mate with the arc-jet sting arm. This compromise was acceptable because the hypersonic nature of the testing means that results are mostly dictated by the fore body geometry. The design was also compromised by constructing the ablative heat shield out of two machined blank blocks of PICA material available at no cost instead of a single continuous shell.

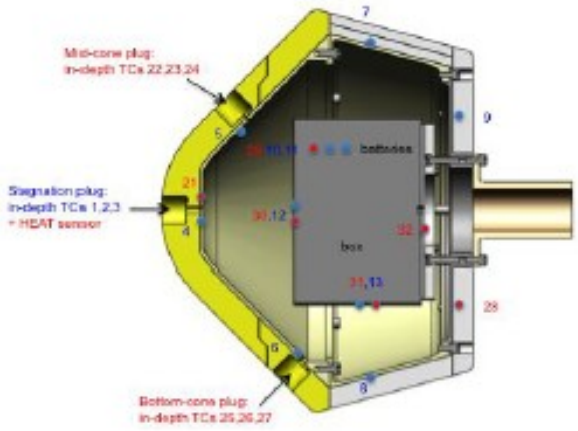

Figure 1.3 – Modified SPRITE geometry for arc-jet testing [13].

The results showed excellent agreement between simulated and actual flow separation on the body, which translates to accurate prediction of aerodynamic forces. The discrepancy in heat flux between test results and simulations can be attributed to two known sources of error; the non-uniformity of bulk enthalpy in the flow from the arc-jet, and the software requirement of uniform inflow initial conditions. The non-uniform bulk enthalpy in the flow from the arc-jet has yet to be characterized and the software is not yet capable of non-uniform inflow conditions [14].

1.3 Objective

The objective of this project is to perform simulations of the SCRAMP probe geometry to characterize the aerothermodynamic properties in Mars entry conditions. With this information, its thermal protection system and planned trajectory can be further refined based on ablative effects.**CHAPTER 2**

SIMULATION SETUP

2.1 Geometry Parameterization

The first step in the approach is to parameterize the geometry of the SCRAMP body and determine an optimal aerodynamic configuration for entry by performing idealized simulations. Simulations in free molecular flow, supersonic and hypersonic flow with disassociating gasses are required to determine optimized geometry. Once optimal geometry is selected, increase detail of geometry and determine aerodynamic characteristics for nominal flight path.

The geometry parameterization completed in MATLAB script to create a data set of two-dimensional coordinates of the desired body profile in axisymmetric form. This provides a complete geometry for the model with any desired parameter of variables, including the following: nose radius, body length, body ramp angle, fin thickness, fin radius (total width), fin shoulder radius, fin start location, gap distance, aft section type (spherical, conical or truncated), and number of data points along each section of the body. Figure 2.1 shows an example graphic output of the script.

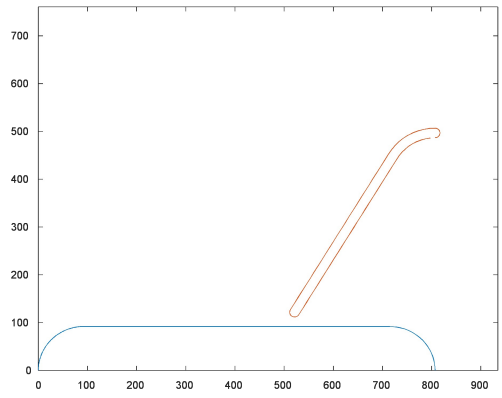

Figure 2.1 – Example Parameterized Axisymmetric Body Geometry.

This data can be used in CAD or grid generating software to create a 3D grid model of the full body by rotating about the center.

2.2 Test Case Selection

The flight path of the probe is dependent on the aerodynamic characteristics yet to be determined, so they follow the flight path of the closest comparison, the DS-2 probes.

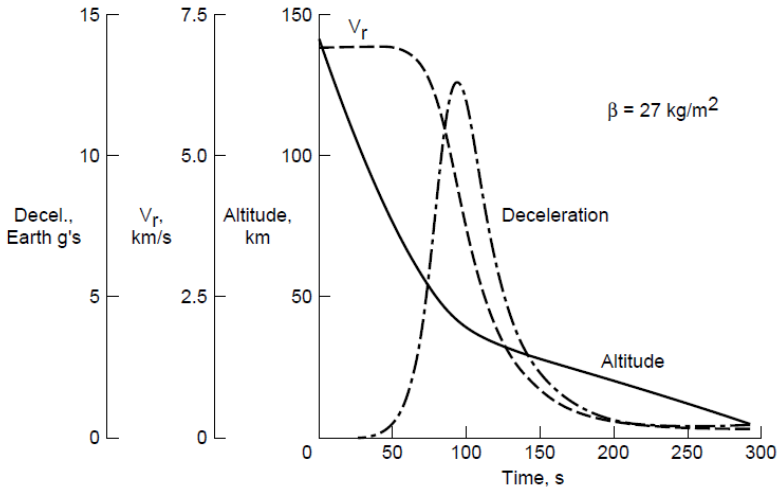

Figure 2.2 – DS-2 Entry Profile [15].

The cases selected best capture the heating and deceleration profile with a limited number of test points available. Free stream conditions are selected from average values which may vary due to high variance in atmospheric properties with respect to seasons and weather.

Table 2.1 – Selected Mars Entry Profile Case Conditions [16].

Case	Alt. (km)	V_∞ (m/s)	T_∞ (K)	P_∞ (Pa)	ρ (kg/m^3)	Q_∞ (Pa)
A	80	7000	129.5	0.046	1.86 E-6	45.57
B	65	6800	143.0	0.361	1.33 E-5	307.5
C	50	6000	157.0	2.25	8.26 E-5	1487
D	35	3000	171.0	13.8	4.25 E-4	1912
E	20	400	185.0	70.1	2.20 E-3	176.0

Five cases were selected initially, but the highest altitude case would not provide satisfactory simulation results due to low temperature and density properties of the free stream flow. The three geometries tested include a “base” case with a straight 45 degree wing, a variation with a 100 mm radius on the fin, and an increased gap size of 50 mm. All use a reference length of .715 meters.

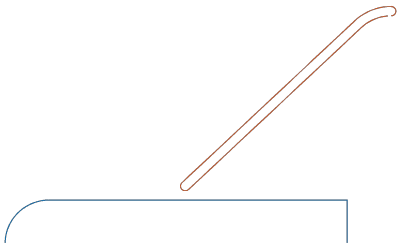

Figure 2.3 – “Base”, “Gap” and “Shoulder” axisymmetric test geometry.

2.3 Navier-Stokes Equations

The simulation of flow around the body of interest is performed by leveraging the Navier-Stokes Equations. By defining a control volume around the body, the basic laws of conservation of mass and energy are applied to the system. The system control volume is divided into finite volumes small enough to accurately predict flow properties and aerodynamic forces on the body [17].

$$\frac{\partial \rho}{\partial t}+\frac{d(\rho u)}{\delta x}+\frac{\delta(\rho v)}{\delta y}+\frac{\delta(\rho w)}{\delta z}=0 \tag{2.1}$$

$$\frac{\partial(\rho u)}{\partial t}+\frac{d(\rho u^2)}{\delta x}+\frac{\delta(\rho uv)}{\delta y}+\frac{\delta(\rho uw)}{\delta z}=\frac{-\delta p}{\delta y}+\frac{1}{\Re}\left[\frac{\delta \tau_{xx}}{\delta x}+\frac{\delta \tau_{xy}}{\delta y}+\frac{\delta \tau_{xz}}{\delta z}\right] \tag{2.2}$$

$$\frac{\partial(\rho v)}{\partial t}+\frac{d(\rho uv)}{\delta x}+\frac{\delta(\rho v^2)}{\delta y}+\frac{\delta(\rho vw)}{\delta z}=\frac{-\delta p}{\delta y}+\frac{1}{\Re}\left[\frac{\delta \tau_{xy}}{\delta x}+\frac{\delta \tau_{yy}}{\delta y}+\frac{\delta \tau_{yz}}{\delta z}\right] \tag{2.3}$$

$$\frac{\partial(\rho w)}{\partial t}+\frac{d(\rho uw)}{\delta x}+\frac{\delta(\rho vw)}{\delta y}+\frac{\delta(\rho w^2)}{\delta z}=\frac{-\delta(up)}{\delta x}+\frac{1}{\Re}\left[\frac{\delta \tau_{xx}}{\delta x}+\frac{\delta \tau_{xy}}{\delta y}+\frac{\delta \tau_{xz}}{\delta z}\right] \tag{2.4}$$

$$\frac{\delta(E_T)}{\delta t}+\frac{\delta(u E_T)}{\delta x}+\frac{\delta(v E_T)}{\delta y}+\frac{\delta(w E_T)}{\delta z}=¿ \tag{2.5}$$

$$\frac{\delta(up)}{\delta x}+\frac{\delta(vp)}{\delta y}+\frac{\delta(\wp)}{\delta z}+\frac{1}{\Re}\left[\frac{\delta}{\delta x}\left(u\tau_{xx}+v\tau_{xy}+w\tau_{xz}\right)+\frac{\delta}{\delta x}\left(u\tau_{xx}+v\tau_{xy}+w\tau_{xz}\right)+\frac{\delta}{\delta x}\left(u\tau_{xx}+\right.\right.$$

To accurately predict properties of the flow in a structured mesh, a cell must have normal faces to preserve the validity of the Navier-Stokes equations. This requirement becomes increasingly difficult to meet with spherical geometries and multiple features on a body. Grids have been simplified greatly by building grids utilizing overlapping Chimera cells on the fin walls in CFD-GEOM.

2.4 Reaction Chemistry

Hypersonic flow encountered in planetary entry will dissociate and partially ionize gases. To accurately model flow around the SCRAMP, the Park-94 model is utilized [15]. This model has been verified in previous axisymmetric Mars entry simulations [19].

$$K_f(T) = A_f T^{b_f} \exp(-E_f/T) \left[m^3 / (kmol \cdot s)\right] \quad (2.6)$$

$$K_r(T) = A_r T^{b_r} \exp(-E_r/T) \left[m^6 / (kmol^2 \cdot s)\right] \quad (2.7)$$

Table 2.2 – Reactions and constants for reaction rates [14].

#	Reaction	A_f	B_f	E_f	A_r	B_r	E_r
1	CO2+O2 <-> CO+O+O	6.90E18	-1.5	63275	1.14E11	-0.75	535
2	CO2+O <-> CO+O+O	1.38E19	-1.5	63275	2.28E11	-0.75	535
3	CO2+C <-> CO+O+C	1.38E19	-1.5	63275	2.28E11	-0.75	535
4	CO2+C <-> CO+CO+O	6.90E18	-1.5	63275	1.14E11	-0.75	535
5	CO2+CO2 <-> CO+O+CO2	6.90E18	-1.5	63275	1.14E11	-0.75	535
6	CO+O2 <-> C+O+O2	2.30E17	-1.0	12900	5.13E12	-1.00	0
7	CO+O <-> C+O+O	3.40E17	-1.0	12900	7.59E12	-1.00	0
8	CO+C <-> C+O+C	3.40E17	-1.0	12900	7.59E12	-1.00	0
9	CO+CO <-> C+O+CO2	2.30E17	-1.0	12900	5.13E12	-1.00	0
10	CO+CO2 <-> C+O+CO2	2.30E17	-1.0	12900	5.13E12	-1.00	0
11	O2+C <-> O+O+C	1.00E19	-1.5	59500	1.00E13	-1.00	0
12	O2+CO <-> O+O+CO	2.00E18	-1.5	59500	2.00E12	-1.00	0
13	O2+CO2 <-> O+O+CO2	2.00E18	-1.5	59500	2.00E12	-1.00	0
14	CO+CO <-> CO2+C	2.33E6	0.5	65710	4.60E9	-0.25	0
15	CO+O <-> O2+C	3.90E10	-0.18	69200	1.34E11	-0.43	0
16	CO2+O <-> O2+CO	2.10E10	0.0	27800	4.11E7	0.50	0
17	O2+O2 <-> O+O+O2	2.00E18	-1.5	59500	2.00E12	-1.00	23800
18	O2+O <-> O+O+O	1.00E19	-1.5	59500	1.00E13	-1.00	0

CHAPTER 3

AERODYNAMIC RESULTS

3.1 Newtonian Approximation

Due to the high entry velocity of the probe, a modified Newtonian approximation of the drag can be performed to calculate an estimate of the drag forces at hypersonic velocities [4]. This is built into the geometry parameterization code due to the nature of this method relying solely on the geometry of the body in axisymmetric flow.

$$C_P = C_{P,Max} \sin^2\Theta \tag{6.1}$$

$$C_{P,Max} = \frac{p_{0,2} - p_\infty}{\frac{1}{2} p_\infty V_\infty^{\,2}} \tag{6.2}$$

$$C_a = \frac{1}{y}\int_0^y C_{P,\leq i} - C_{P,TE}\, dy \tag{6.3}$$

3.2 Simulation Results

Computational results of the axisymmetric simulations provide three dimensional axial force coefficients. The passively stable nature of the planned trajectory assumes little or no angle of attack.

Table 3.1 – Axial force coefficient results.

	Reference Area (m^2)	C_a Newtonian	C_a B	C_a C	C_a D	C_a E
Base	0.807	0.986	.749	0.884	0.957	0.908
Gap	0.906	0.930	1.037	0.919	1.070	1.188
Shoulder	0.807	0.950	.704	.899	0.902	0.873

3.2 Analysis

Cases in which the shock layer is deflected entirely by the wing section exhibit properties similar to a conventional reentry geometry as shown in Figure 3.1. A higher drag coefficient is experienced in conditions where the shock layer partially flows through the gap section, seen in figure 3.2. This can be explained by viscous interactions behind the shock. Temperature profiles of the flow at the wall also appear much higher in these cases. These characteristics may vary greatly with different geometry at the aft section of the body in future work.

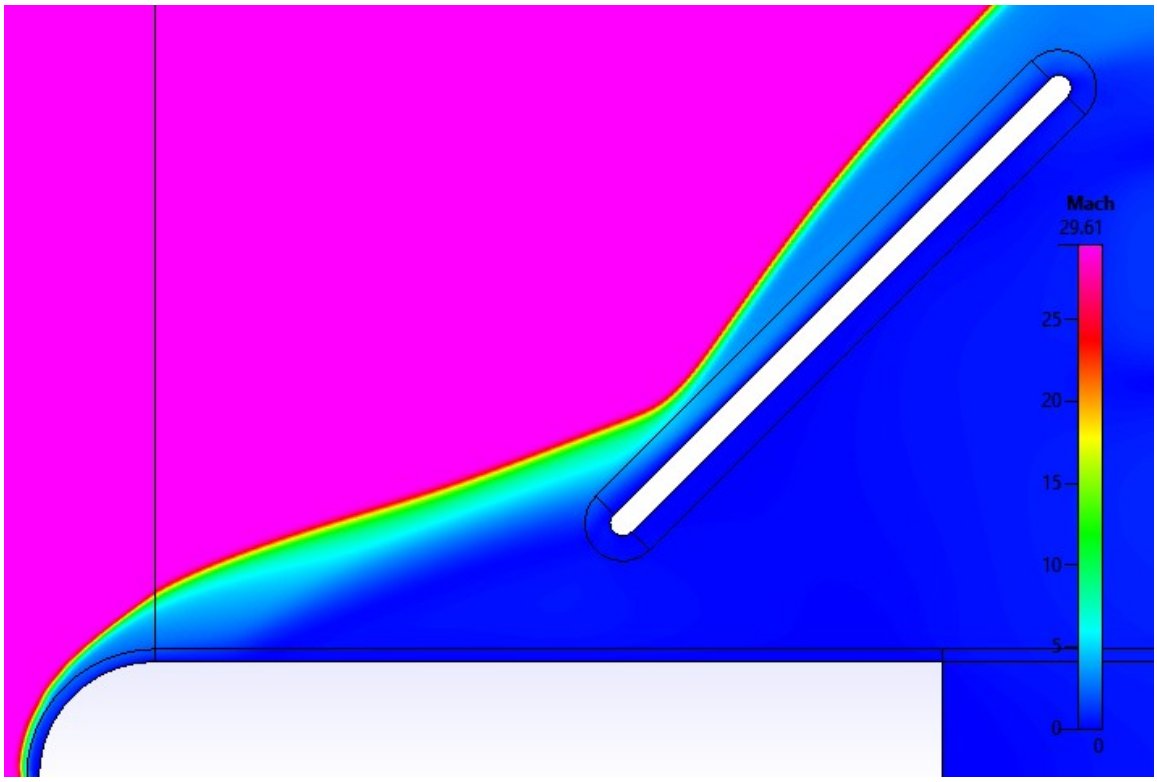

Figure 3.1 – Gap case C Mach contour.

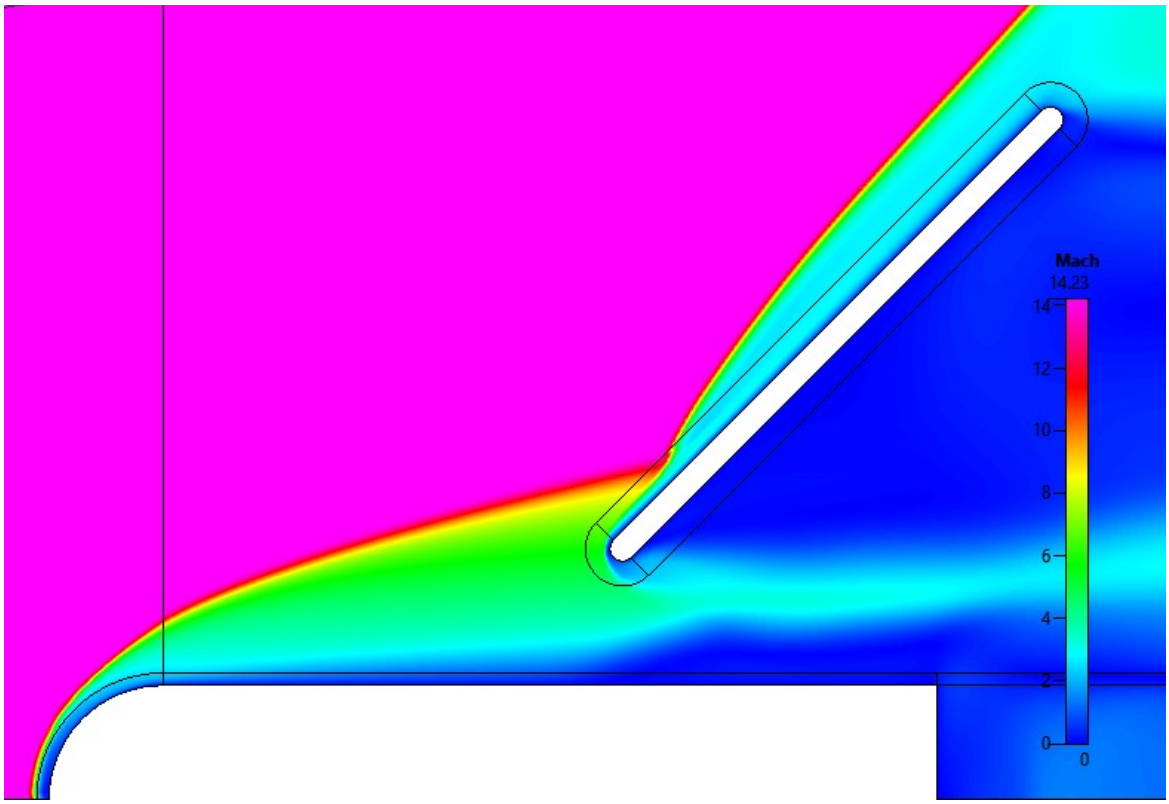

Figure 3.2 – Gap case D Mach contour.

Desirable aerodynamic characteristics may vary based on the planned trajectory. A higher drag design may benefit cases where atmospheric temperatures are relatively low. Lower drag designs would be more beneficial for high velocity entries in which the total heat load is required to be minimized.

CHAPTER 4

THERMAL PROPERTIES

4.1 Stagnation Point Heating

The point of greatest interest with respect to heating and ablation is the stagnation point on the hemispherical nose since it experiences the greatest effects and can be used to estimate other conditions. The Sutton-Graves heating equation provides an approximation for convective stagnation point heat flux on a spherical forebody entering Mars atmosphere [5].

$$q_{convective} = 1.9027 \times 10^{-4} \sqrt{\frac{\rho_{\infty}}{R_{nose}}} V_{\infty}^{3} \tag{4.1}$$

Table 4.1 – Stagnation point heat flux approximation.

Test Case	A	B	C	D	E
q (W/cm^2)	29.3	71.9	123	34.9	0.188

These values can be curve fit and integrated to provide the total stagnation point heat load with refined results. Current calculations assume all significant heat flux to occur over 100 to 150 seconds as shown in other Mars entry profiles.

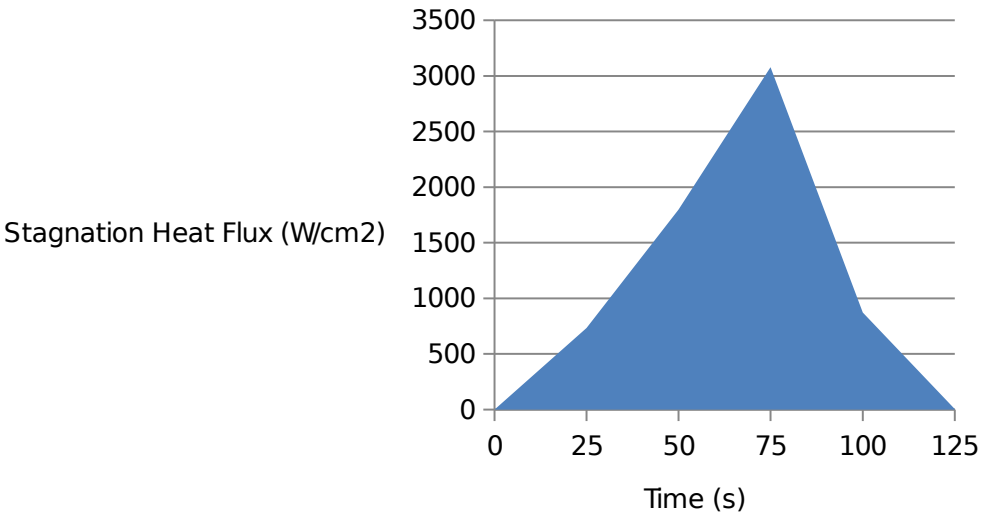

Figure 4.1 – Heat pulse approximation.

Table 4.2 - Comparison of small probe thermal properties.

Probe	Mass (kg)	Stagnation Point Heat Load (J/cm²)	Peak Heat Flux (W/cm²)	Peak Deceleration (G)	Ballistic Coefficient (kg/m²)
DS-2	2.5	7,165	200	12.6	27
Beagle 2	60	2,100	75	15	70
Stardust	45.8	30,000	1100	34	13
Genesis	193	16,750	515	27.2	70
SCRAMP	*20*	*6,490*	*123*	*TBD*	*41*

4.2 Analysis

The values obtained through Sutton-Graves calculations appear to be proportional to comparable Mars entry missions. Although heating calculations for the spherical nose are identical since there was no variation in the fore body radius parameter, heating characteristics vary in simulations on the wing surface. It should be noted that the wing section of the geometry

experiences temperatures very similar to the stagnation point. In cases where the shock layer captured by the wing section, flow density is nearly equal to that of the stagnation point as shown in Figure 4.2. The highest density in the flow occurs at the shock-shock interaction at a small distance from the wall.

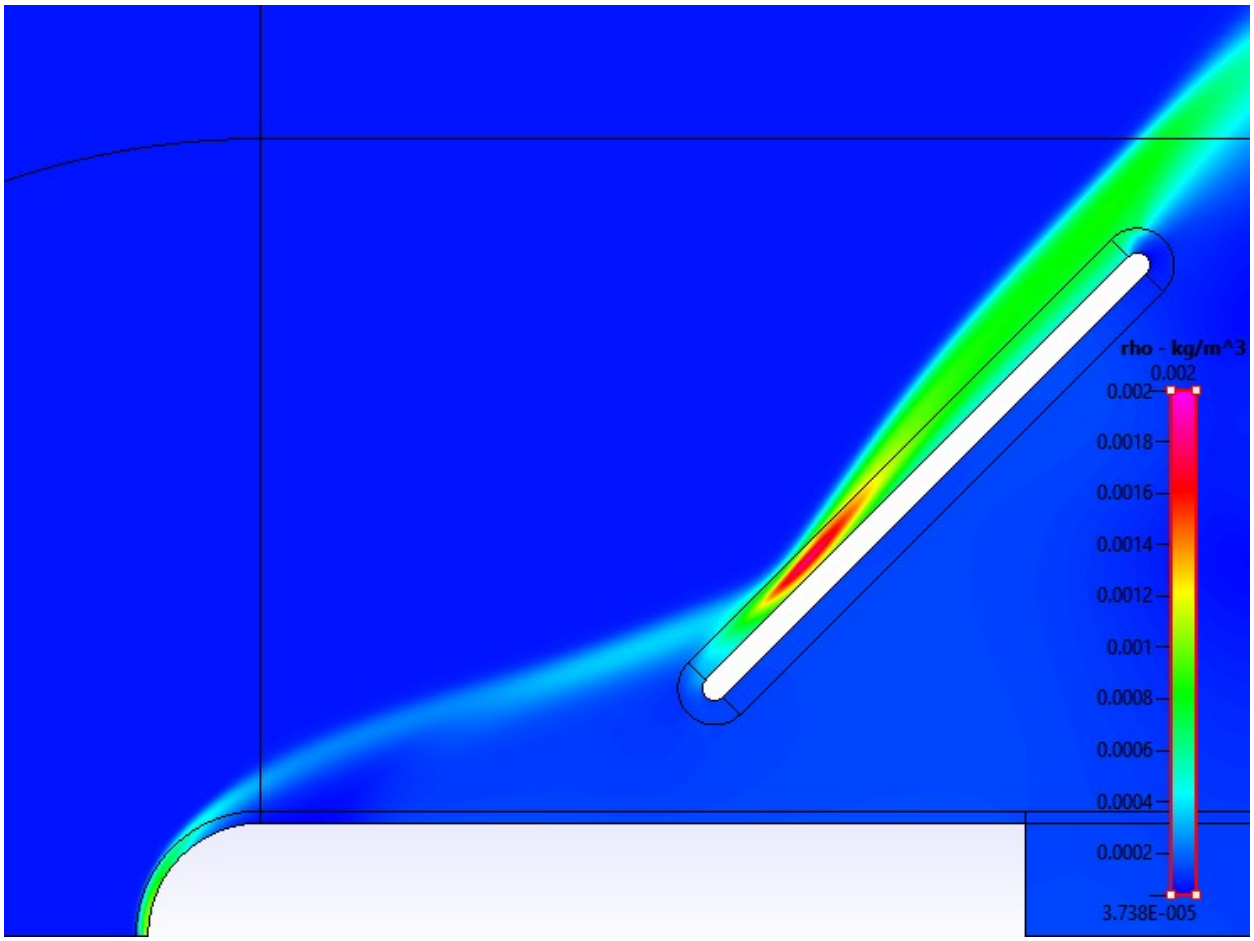

Figure 4.2 – Gap case C density contour

These properties of the flow show that ablative analysis should be performed on the wing surface as well as the spherical nose. Analysis using ablative material in the fore body in a similar Mars entry study reduced the max heating rate by roughly 50 percent, while use of ablative material on the trailing side had a negligible effect [5].

CHAPTER 5

CONCLUSION

This analysis has provided aerodynamic and thermal properties suitable for a first iteration of a mission design. For mission specific analysis, two or more design iterations would be ideal. In addition to ablation analysis, Monte Carlo simulations would be valuable due to uncontrollable atmospheric interface conditions and variable atmospheric properties including temperature, pressure, species and dust composition. Use of Monte-Carlo simulations in combination with CFD simulations has been shown to provide results accurate to mission experiments [11]. These results can also be used to refine future simulations by designing grids to capture the shock layer and shock-shock interactions in closer detail.

REFERENCES

1 Zubrin, R., *The Case for Mars*, Simon and Schuster, 2012.

2 Zuniga, D., Murbach, M. A., Leimkuehler, T. O., Leidich, J., Chiesi, S. S., Conceptual Development of a Payload Thermal and Pressure Control System for a Small Payload Quick Return Vehicle, *40th International Conference on Environmental Systems*, Jul. 2010.

3 Papadopoulou, E., *Numerical Simulations of the Apollo 4 Re-entry Trajectory* (Doctoral dissertation, École Polytechnique Federale de Lausanne), 2014.

4 Anderson, J. D., *Hypersonic and High Temperature Gas Dynamics*, AIAA, 2010.

5 Mitcheltree, R. A., Moss, J. N., Cheatwood, F. M., Greene, F. A., Braun, R. D., Aerodynamics of the Mars Microprobe Entry Vehicles, *Journal of Spacecraft and Rockets*, Vol. 36, No. 3, 1999, pp. 392-398

6 Liever, P. A., Habchi, S. D., Burnell, S. I., Lingard, J. S., Computational Fluid Dynamics Prediction of the Beagle 2 Aerodynamic Database, *Journal of Spacecraft and Rockets*, Vol. 40, No. 5, 2003, pp. 632-638.

7 Mitcheltree, R. A., Wilmoth, R. G., Cheatwood, F. M., Brauckmann, G. J., Greene, R. A., Aerodynamics of Stardust Sample Return Capsule, *Journal of Spacecraft and Rockets*, Vol. 36, No. 3, 1999.

8 Desai, P. N., Qualls, G. D., Schoenenberger, M., Reconstruction of the Genesis Entry. *Journal of Spacecraft and Rockets*, Vol. 45, No. 1, 2008.

9 Spencer, D. A., Blanchard, R. C., Braun, R. D., Kallemeyn, P. H., Thurman, S. W., Mars Pathfinder Entry, Descent, and Landing Reconstruction. *Journal of Spacecraft and Rockets*, Vol. 36, No. 3, 1999.

10 Gnoffo, P. A., Braun, R. D., Weilmuenster, K. J., Mitcheltree, R. A., Engelund, W. C., Powell, R. W., Prediction and Validation of Mars Pathfinder Hypersonic Aerodynamic Database. *Journal of Spacecraft and Rockets*, Vol. 36, No. 3, 1999.

11 Weaver, A. B., Alexeenko, A. A., Greendyke, R. B., Camberos, J. A., Flowfield Uncertainty Analysis for Hypersonic Computational Fluid Dynamics Simulations. *Journal of Thermophysics and Heat Transfer*, Vol. 25, No. 1, 2011.
12 Empey, D. M., Gorbunov, S., Skokova, K. A., Agrawal, P., Swanson, G. T., Prabhu, D. K., & Venkatapathy, E., Small Probe Reentry Investigation for TPS Engineering (SPRITE). *AIAA Paper*, 2012.
13 Prabhu, D., Flowfield Analysis of a Small Entry Probe (SPRITE) Tested in an Arc Jet. In *50th AIAA Aerospace Sciences Meeting Including the New Horizons Forum and Aerospace Exposition*, Jan. 2012.
14 Braun, R. D., Mitcheltree, R. A., Cheatwood, F. M., Mars Microprobe Entry Analysis, Proc., *IEEE Aerospace Conference Proc., IEEE*, Feb. 1997.
15 *Models of Mars' Atmosphere, NASA TM 19750011035,* NASA GSFC, 1974.
16 Anderson, J. D., Wendt, J., *Computational Fluid Dynamics*, McGraw-Hill, 1995.
17 Park, C., Howe, J. T., Jaffe, R. L., Candler, G. V., Review of Chemical-Kinetic Problems of Future NASA Missions, II: Mars Entries. *Journal of Thermophysics and Heat Transfer*, Vol. 8, No. 1, 1994, pp. 9-23.
18 Vinteler, D., Megahed, M., Blosch, E., Numerical Prediction for Mars Atmosphere Entry Vehicle Using a Density Based Solver. In *Radiation of High Temperature Gases in Atmospheric Entry*, Vol. 629, Nov. 2006.

APPENDIX A

SIMULATION SURFACE PLOTS

Case B – Near Body

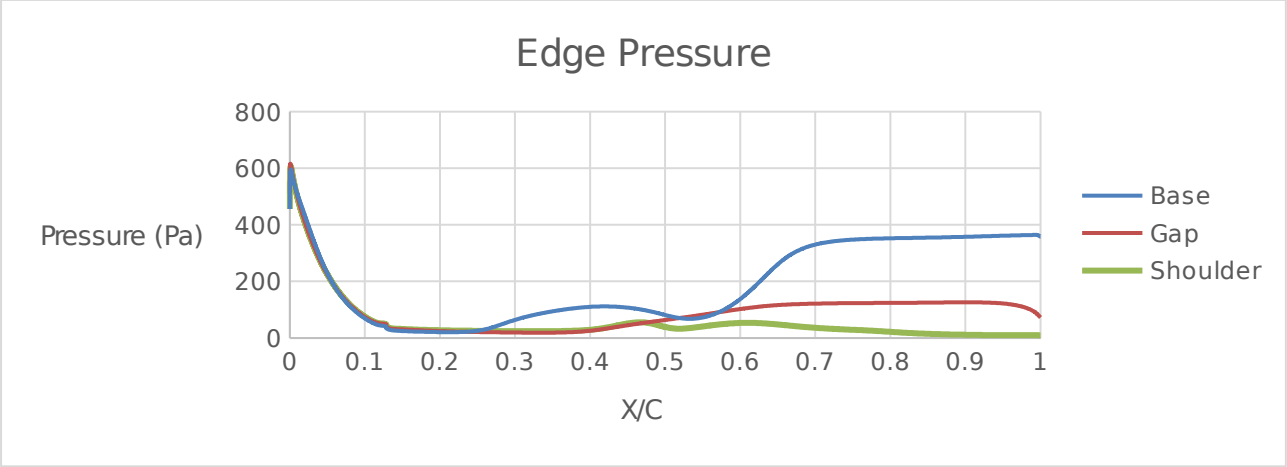

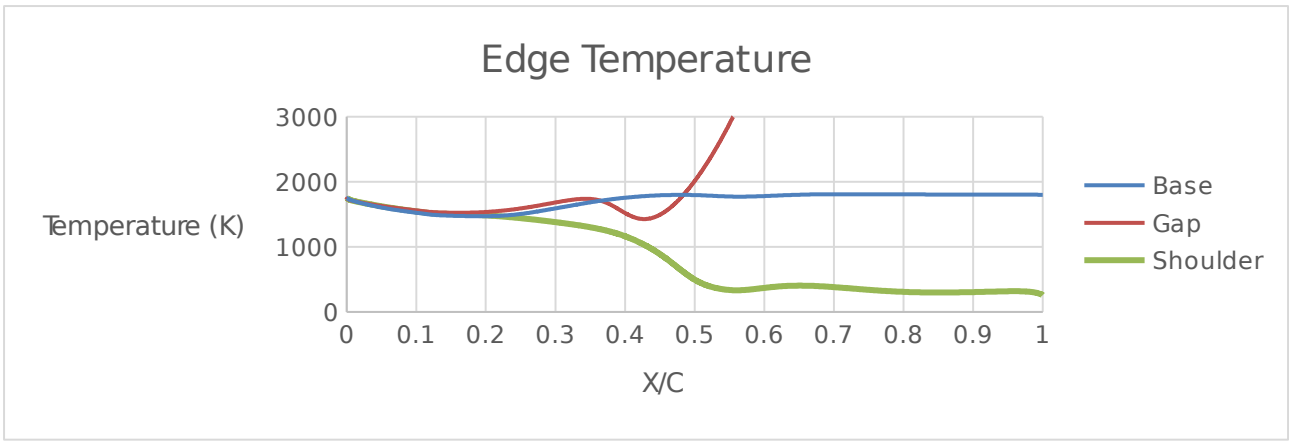
Edge Temperature
Temperature (K)
3000
2000
1000
0
0
0.1
0.2
0.3
0.4
0.5
0.6
0.7
0.8
0.9
1
X/C
Base
Gap
Shoulder

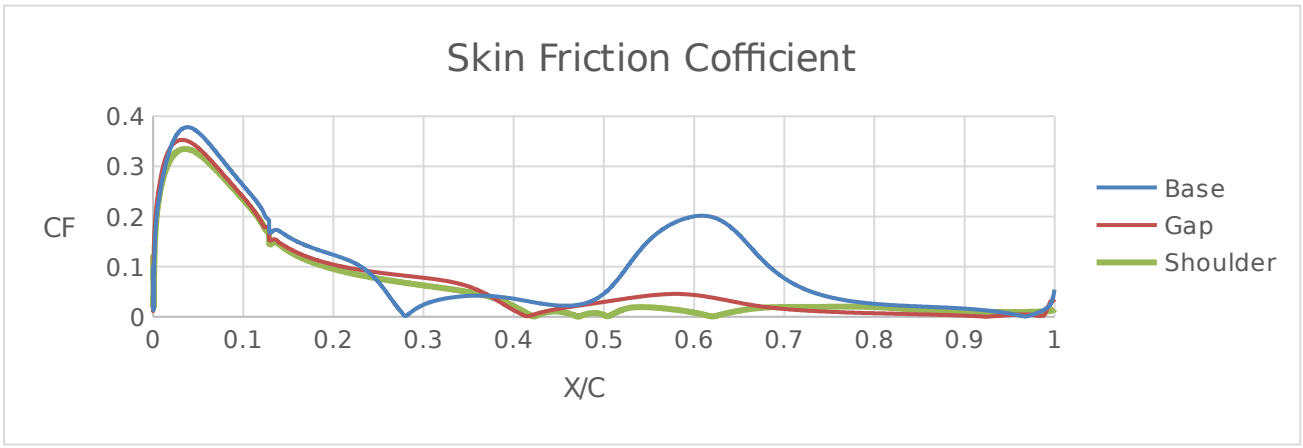
Skin Friction Cofficient
CF
0.4
0.3
0.2
0.1
0
0
0.1
0.2
0.3
0.4
0.5
0.6
0.7
0.8
0.9
1
X/C
Base
Gap
Shoulder

Case B – Near Wing

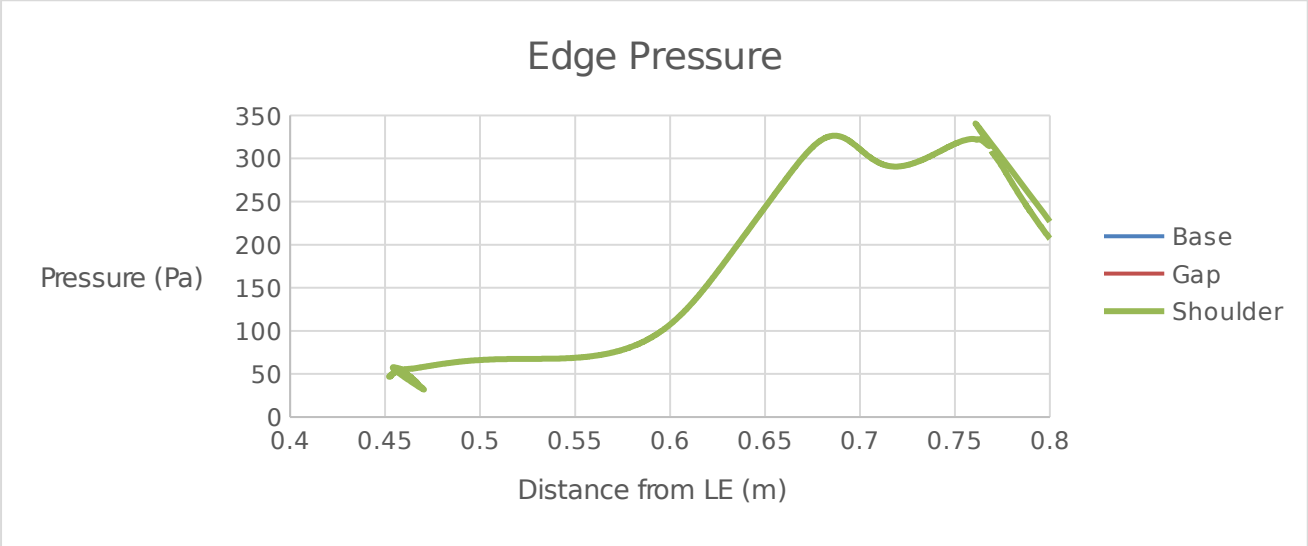

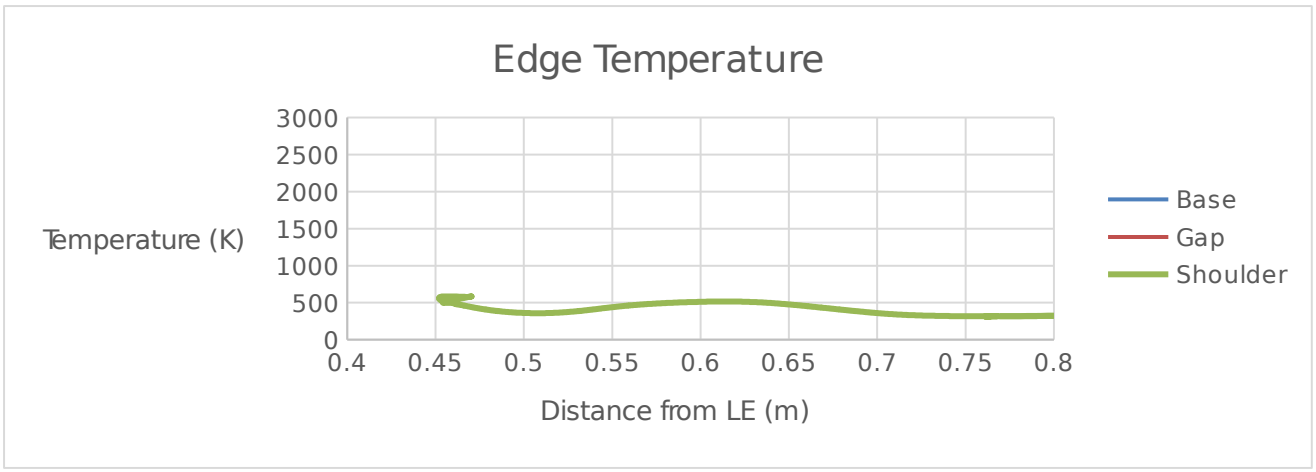
Edge Temperature
Temperature (K)
3000
2500
2000
1500
1000
500
0
0.4
0.45
0.5
0.55
0.6
0.65
0.7
0.75
0.8
Distance from LE (m)
Base
Gap
Shoulder

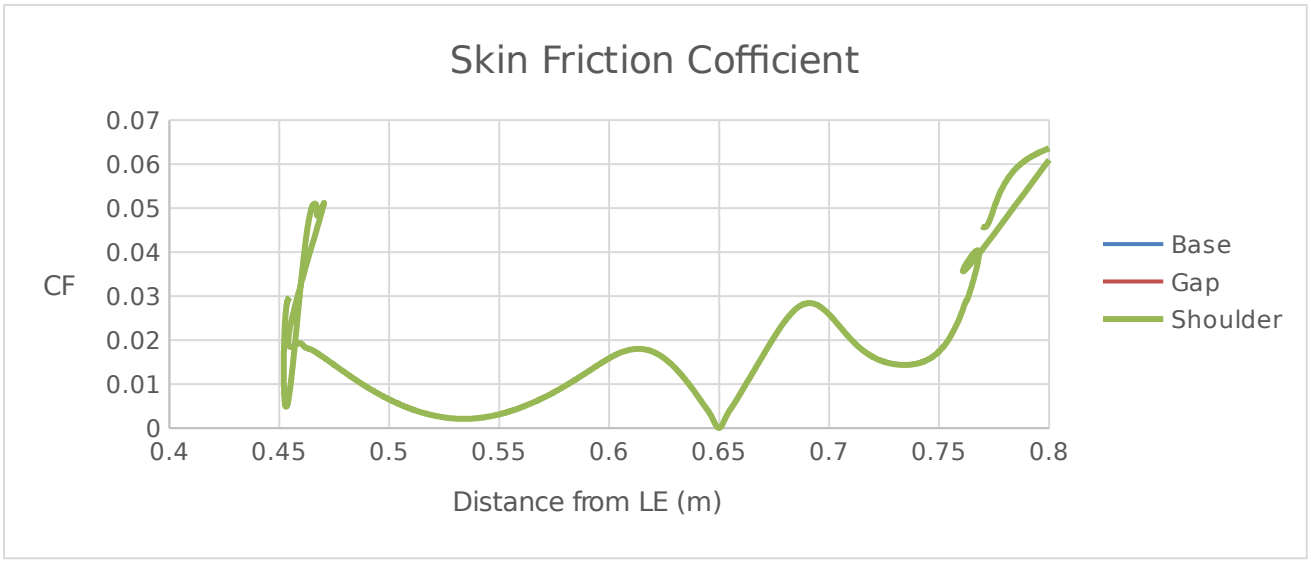
Skin Friction Cofficient
CF
0.07
0.06
0.05
0.04
0.03
0.02
0.01
0
0.4
0.45
0.5
0.55
0.6
0.65
0.7
0.75
0.8
Distance from LE (m)
Base
Gap
Shoulder

Case C – Near Body

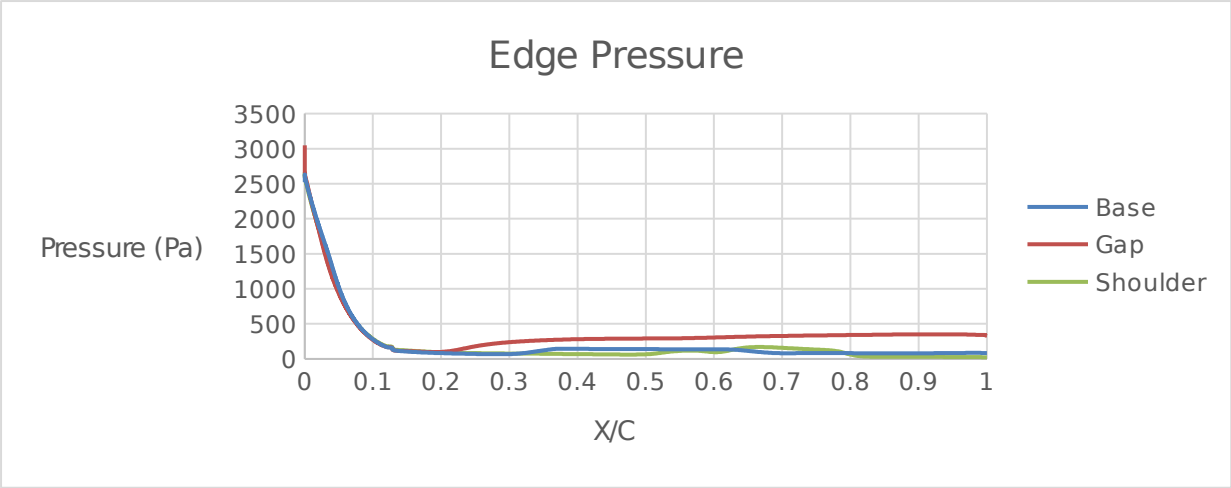
Edge Pressure
Pressure (Pa)
3500
3000
2500
2000
1500
1000
500
0
0
0.1
0.2
0.3
0.4
0.5
0.6
0.7
0.8
0.9
1
X/C
Base
Gap
Shoulder

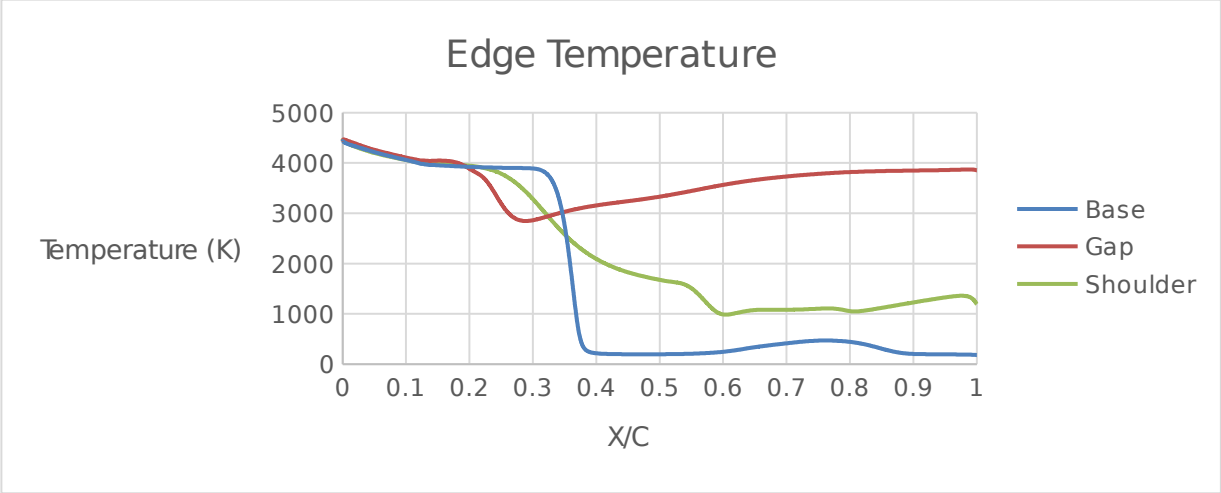
Edge Temperature
Temperature (K)
5000
4000
3000
2000
1000
0
0
0.1
0.2
0.3
0.4
0.5
0.6
0.7
0.8
0.9
1
X/C
Base
Gap
Shoulder

Case C – Near Wing

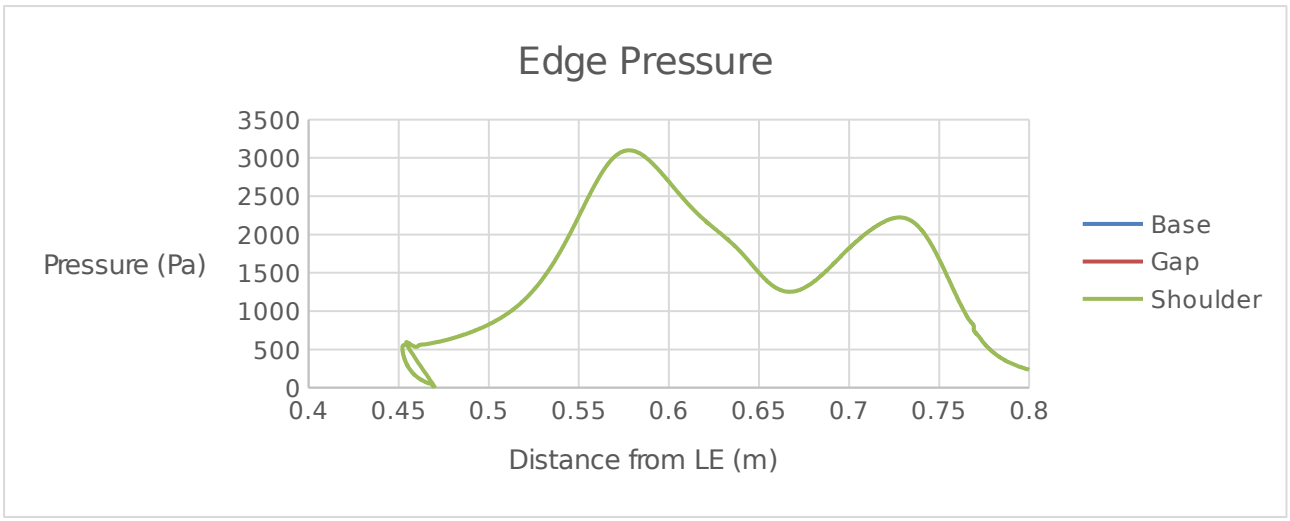
Edge Pressure
Pressure (Pa)
3500
3000
2500
2000
1500
1000
500
0
0.4
0.45
0.5
0.55
0.6
0.65
0.7
0.75
0.8
Distance from LE (m)
Base
Gap
Shoulder

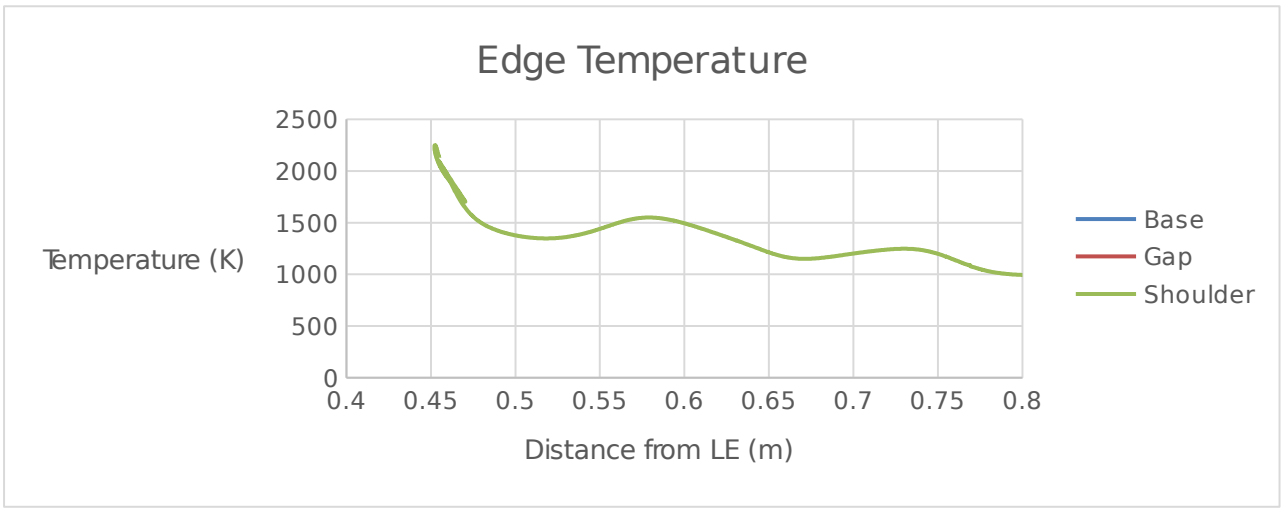
Edge Temperature
Temperature (K)
2500
2000
1500
1000
500
0
0.4
0.45
0.5
0.55
0.6
0.65
0.7
0.75
0.8
Distance from LE (m)
Base
Gap
Shoulder

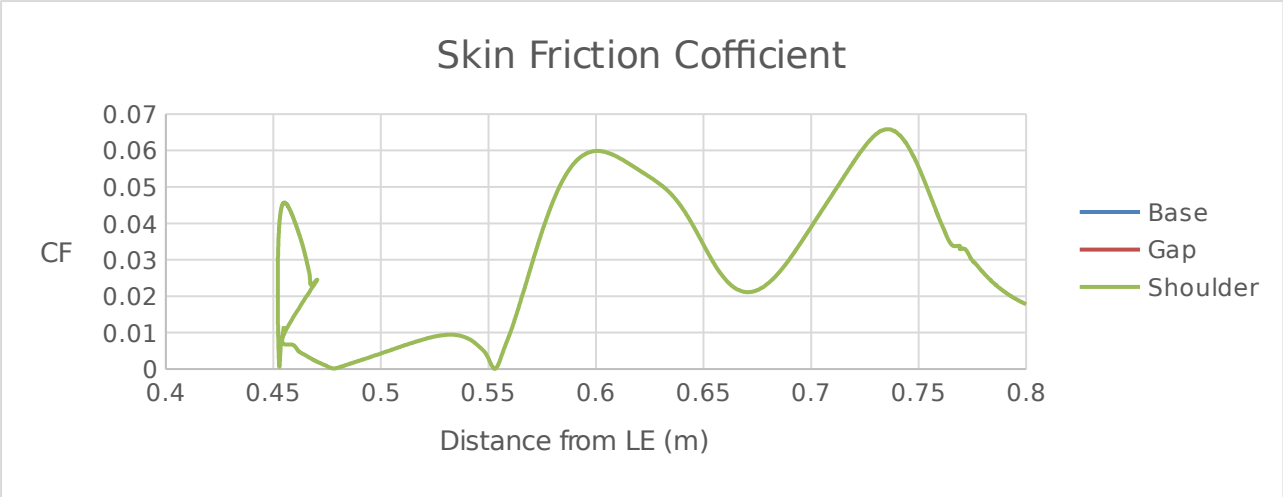

Case D – Near Body

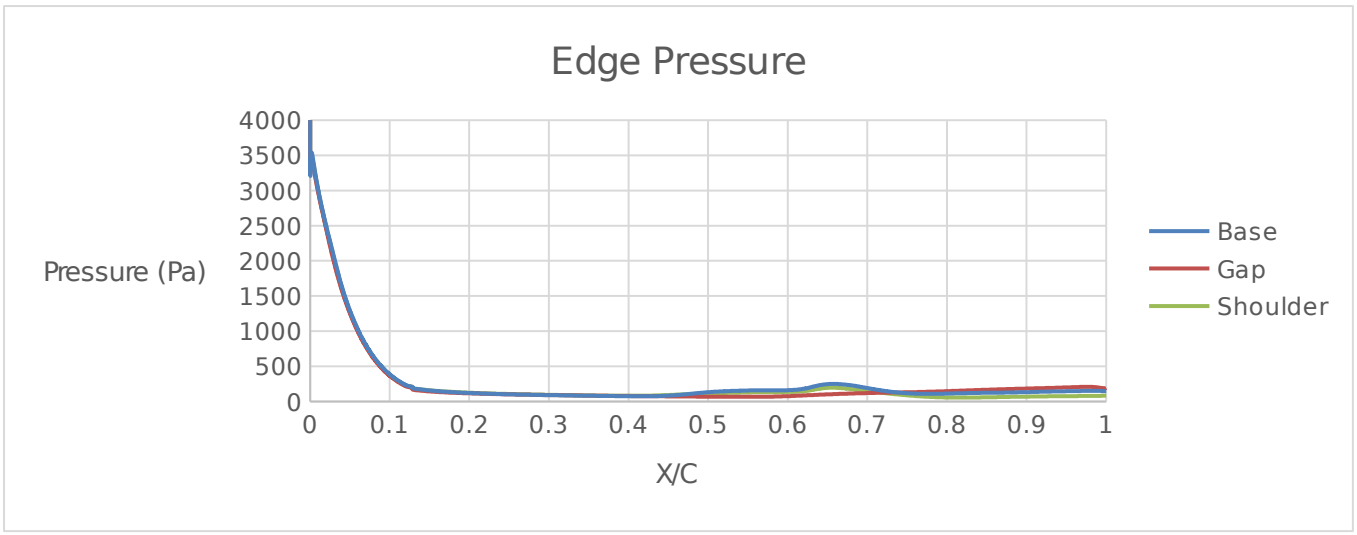
Edge Pressure
Pressure (Pa)
4000
3500
3000
2500
2000
1500
1000
500
0
0
0.1
0.2
0.3
0.4
0.5
0.6
0.7
0.8
0.9
1
X/C
Base
Gap
Shoulder

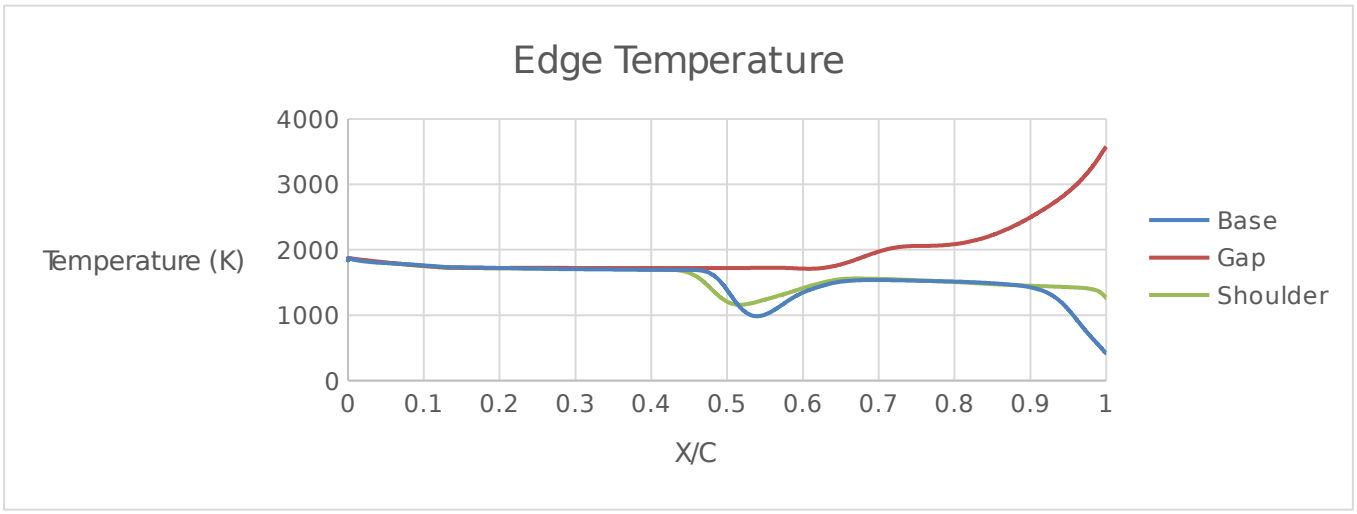
Edge Temperature
Temperature (K)
4000
3000
2000
1000
0
0
0.1
0.2
0.3
0.4
0.5
0.6
0.7
0.8
0.9
1
X/C
Base
Gap
Shoulder

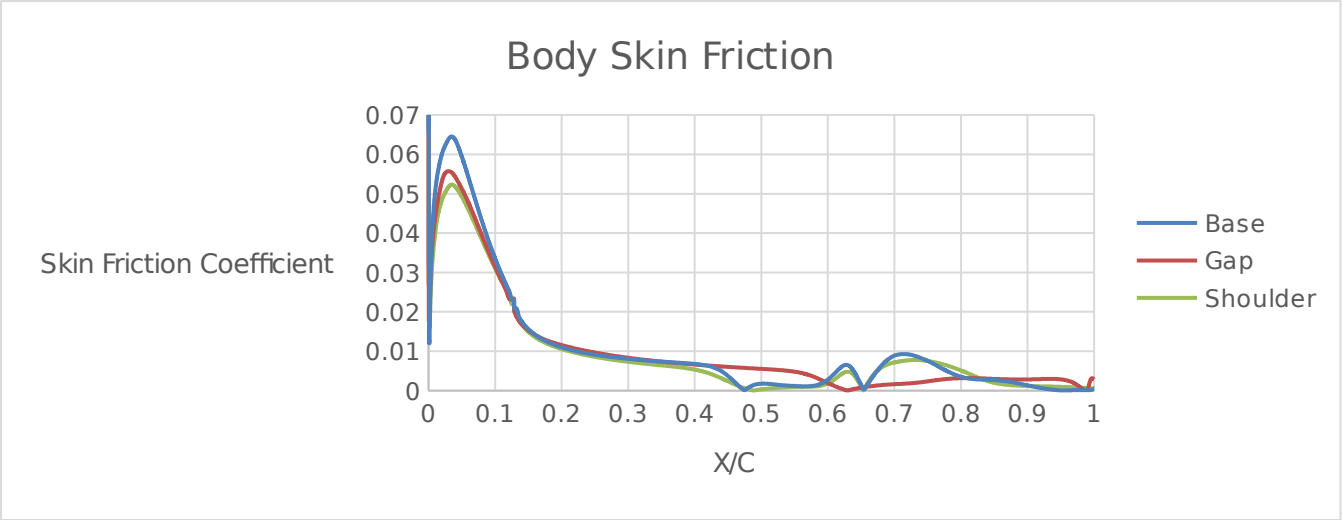

Case D – Near Wing

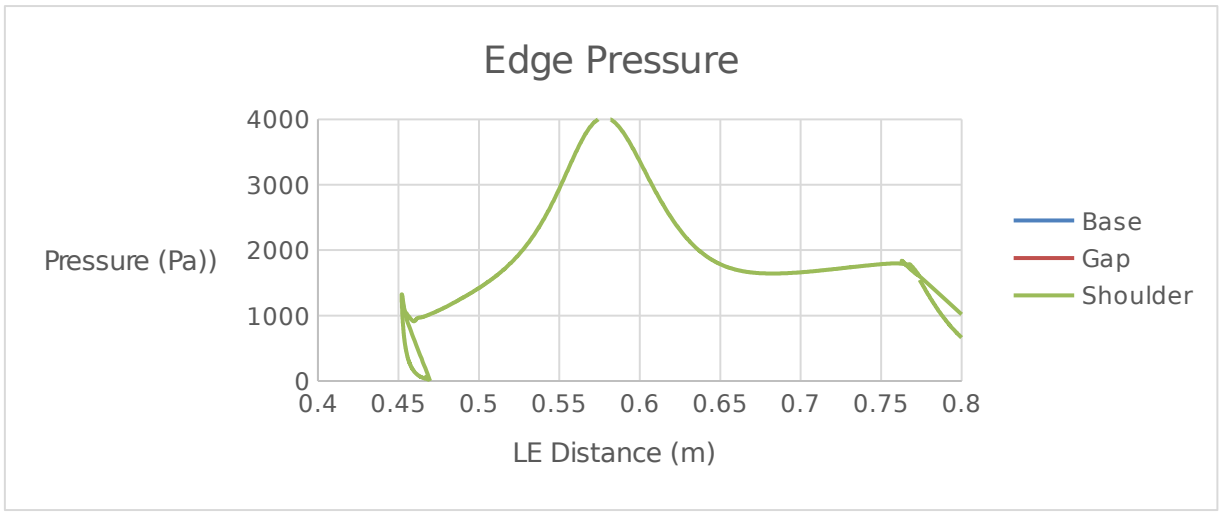
Edge Pressure
Pressure (Pa))
4000
3000
2000
1000
0
0.4
0.45
0.5
0.55
0.6
0.65
0.7
0.75
0.8
LE Distance (m)
Base
Gap
Shoulder

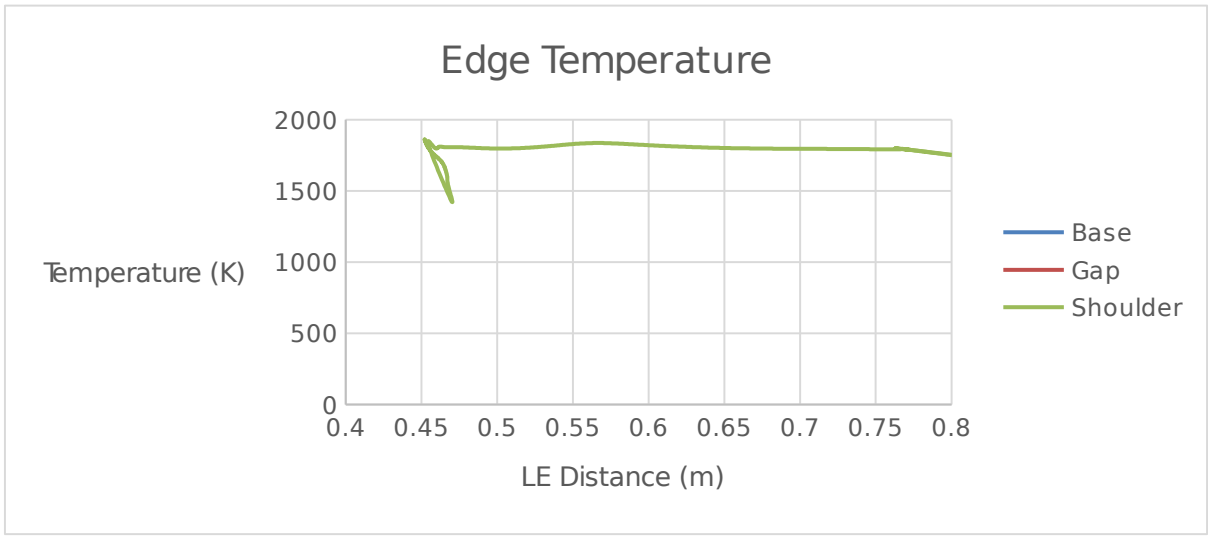
Edge Temperature
Temperature (K)
2000
1500
1000
500
0
0.4
0.45
0.5
0.55
0.6
0.65
0.7
0.75
0.8
LE Distance (m)
Base
Gap
Shoulder

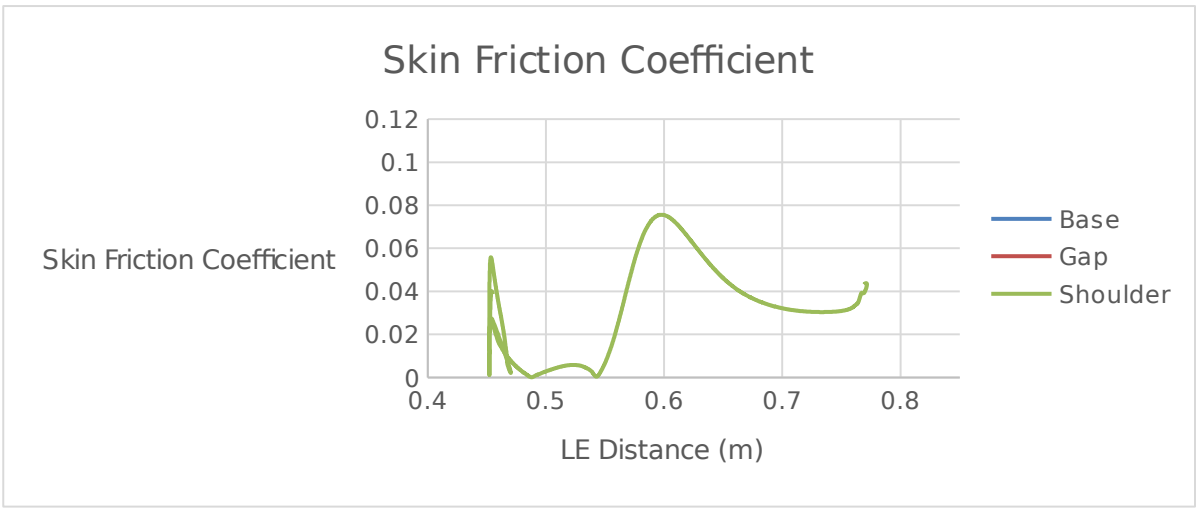

Case E – Near Body

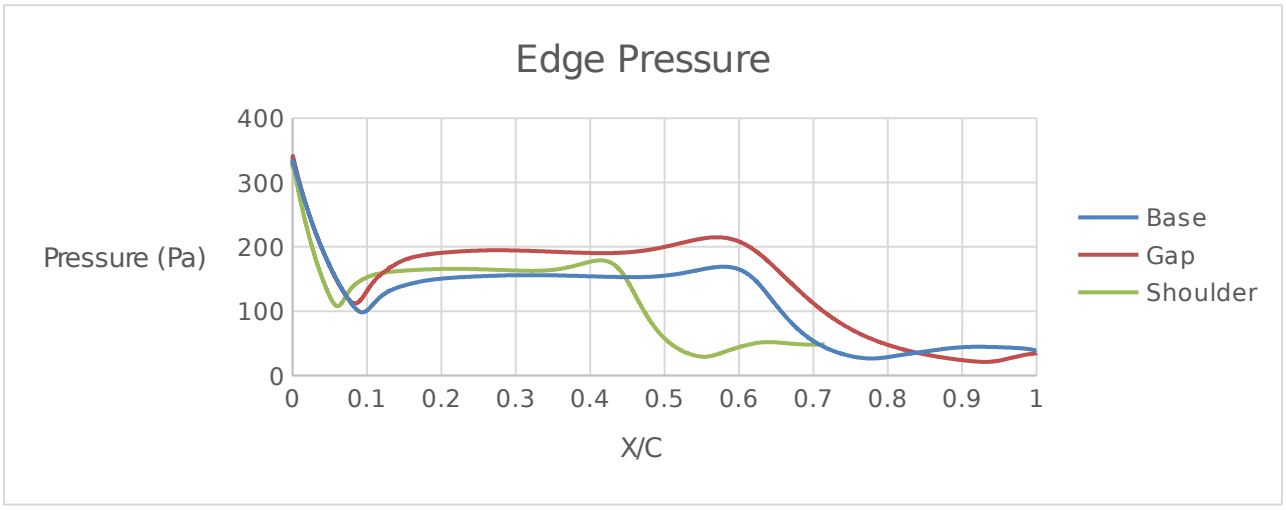

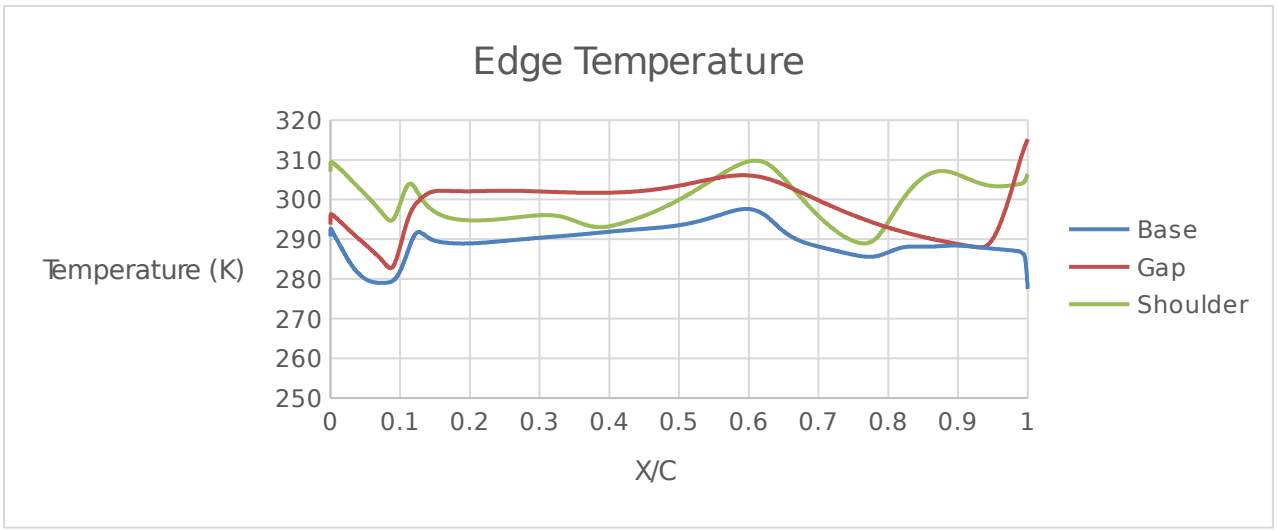
Edge Temperature
Temperature (K)
320
310
300
290
280
270
260
250
0
0.1
0.2
0.3
0.4
0.5
0.6
0.7
0.8
0.9
1
X/C
Base
Gap
Shoulder

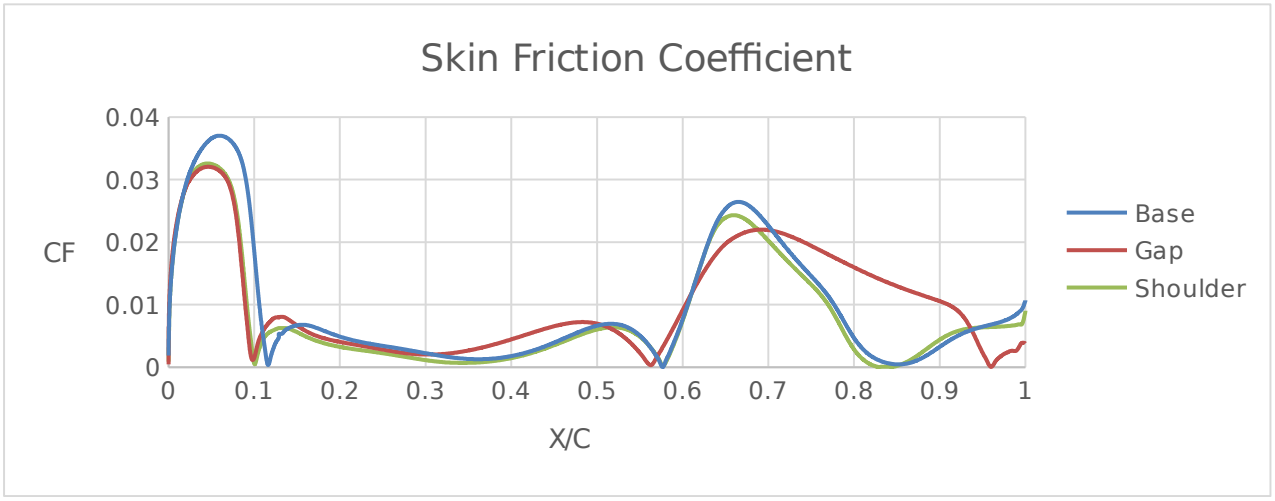
Skin Friction Coefficient
CF
0.04
0.03
0.02
0.01
0
0
0.1
0.2
0.3
0.4
0.5
0.6
0.7
0.8
0.9
1
X/C
Base
Gap
Shoulder

Case E – Near Wing

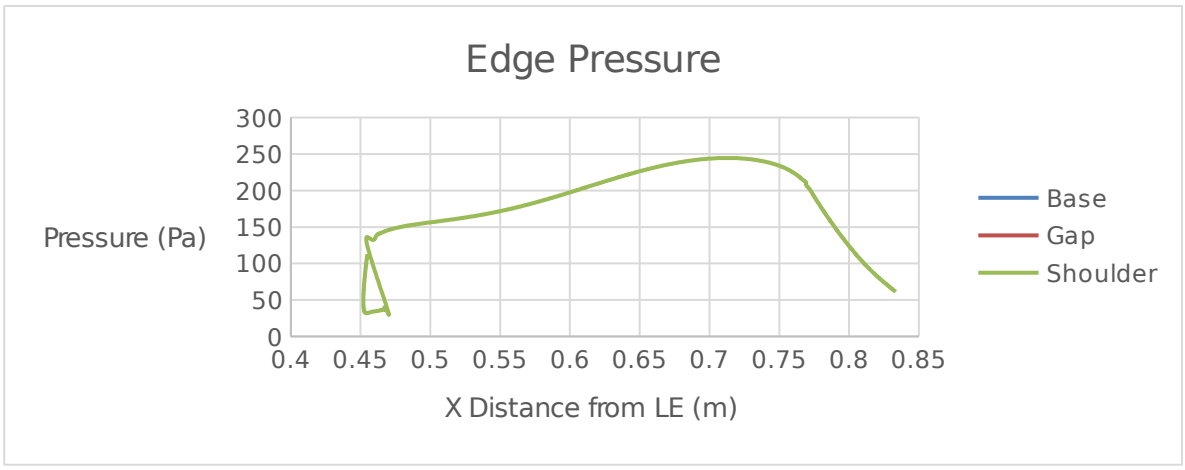
Edge Pressure
Pressure (Pa)
300
250
200
150
100
50
0
0.4 0.45 0.5 0.55 0.6 0.65 0.7 0.75 0.8 0.85
X Distance from LE (m)
Base
Gap
Shoulder

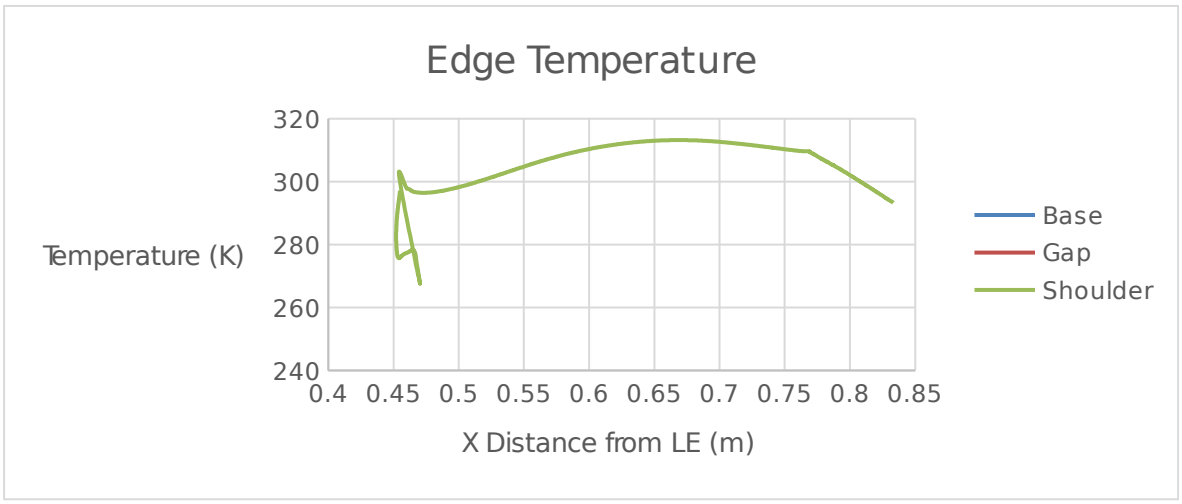
Edge Temperature
Temperature (K)
320
300
280
260
240
0.4 0.45 0.5 0.55 0.6 0.65 0.7 0.75 0.8 0.85
X Distance from LE (m)
Base
Gap
Shoulder

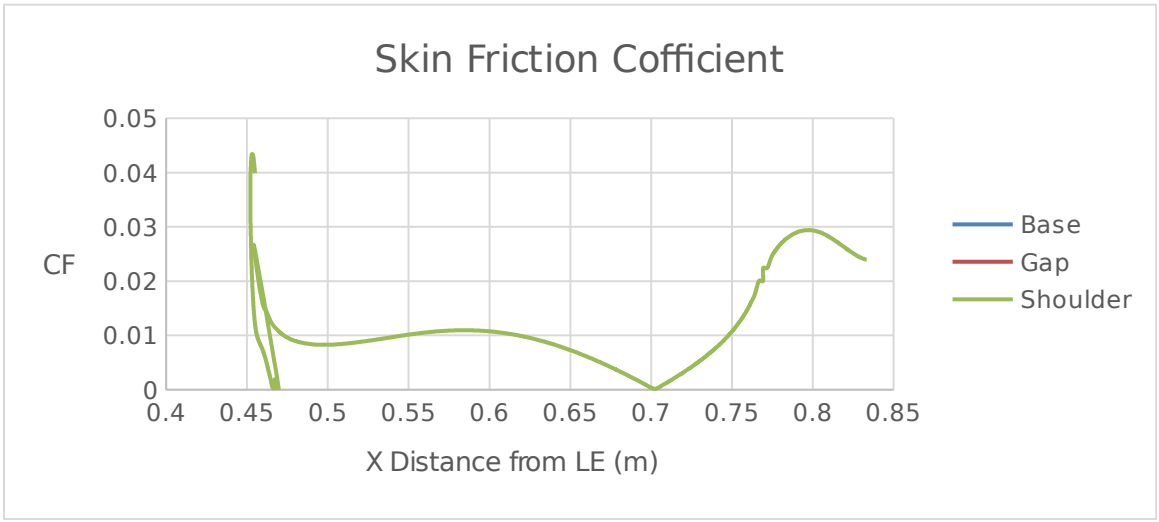
Skin Friction Cofficient
CF
0.05
0.04
0.03
0.02
0.01
0
0.4 0.45 0.5 0.55 0.6 0.65 0.7 0.75 0.8 0.85
X Distance from LE (m)
Base
Gap
Shoulder

APPENDIX B

BODY PARAMETERIZATION MATLAB SCRIPT

```
% TDRV  = [Nose Radius,     # points on nose radius
%          Body Length,     # points on cyl body
%          Body Angle,      # points on fin
%          Fin Angle,         Fin Radius
%          Shoulder Radius, # points on shoulder
%          Gap Distance,      Fin Thickness
%          Aft type - note  # points on aft
%          #Points rear shoulder      0           ]
%
%  TDRV  =   [R_nose,  n_nose;
%             l_body,  n_body;
%             t_body,  n_fin;
%             t_fin,   r_fin;
%             r_shld,  n_shld;
%             d_gap,   d_fin
%             n_shld2, n_aft
%             aft,     0
%             n_shld2         ]
%
%  aft code
%  0    none
%  1    spherical
%  2    conical
%  3    straight
clear all
clc
TDRV = [92   100;     % Nose Radius   n Points on Nose
        623  20;      % Body Length   n Points on Body
        0    25;      % Body Angle    n Points on Fin
        45   507;     % Fin Angle     Total Body radius
        0    10;      % shld radius   n points on shoulder
        20   10;       % Gap distance  Fin Rad / half thickness
        3    20;       % Aft type      n Points aft section
        5    0];      % n rear shoulder  blank - Units in M

Cpmax  = 1.87;

r_nose = TDRV(1,1); n_nose = TDRV(1,2);
l_body = TDRV(2,1); n_body  = TDRV(2,2);
t_body = TDRV(3,1); n_fin  = TDRV(3,2);
t_fin  = TDRV(4,1); r_fin  = TDRV(4,2);
r_shld = TDRV(5,1); n_shld = TDRV(5,2);
d_gap  = TDRV(6,1); d_fin  = TDRV(6,2);
aft    = TDRV(7,1); n_aft  = TDRV(7,2);
n_shld2= TDRV(8,1);

offset = 0; %

for n = 1:1:n_nose
theta_nose(n) = (n-1)*90/(n_nose-1);
x_nose(n) = r_nose - r_nose*cosd(theta_nose(n));
```

```
y_nose(n) = r_nose*sind(theta_nose(n));
end


for n= 1:1:n_body
x_body(n) = r_nose + n * l_body/n_body;
y_body(n) = r_nose + n * l_body*tand(t_body)/n_body;
end

if aft == 1
    disp('Spherical aft body')
    xafthinge = x_body(n_body);
    yafthinge = 0;
    r_aft = r_nose + l_body*sind(t_body);
    for n = 1:1:n_aft
        theta_aft(n) = (n-1)*90/(n_aft-1);
        x_aft(n) = xafthinge + r_aft*sind(theta_aft(n));
        y_aft(n) = r_aft*cosd(theta_aft(n));
    end
elseif aft == 2
    disp('Conical aft body')
    r_aft = r_nose + l_body*sind(t_body);
    for n = 1:1:n_aft
        x_aft(n) = x_body(n_body) + r_aft * (n/n_aft);
        y_aft(n) = y_body(n_body) - r_aft * (n/n_aft);
    end
elseif aft == 3
    disp('Straight aft body')
    for n=1:1:n_aft
       x_aft(n) = x_body(n_body);
       y_aft(n) = y_body(n_body) *(1 - (n/n_body) );
    end
else
    disp('Aft input not valid')
end

% Start and End Centerpoints for fin radius
SBx = l_body + 2*r_nose;
SBy = r_fin-d_fin;
SAy = r_nose + tand(t_body)*offset + d_fin + d_gap;
SAx = SBx - (SBy - SAy)/tand(t_fin);


if r_shld == 0     %**********Straight Fin Generation*********************
for n = 1:1:n_shld+1       % Leading side fin tip (A)
    t_shld(n) = t_fin - 90 - 180*(n-1)/n_shld;
    xtipa(n) = SAx + d_fin*cosd(t_shld(n));
    ytipa(n) = SAy + d_fin*sind(t_shld(n));
end
    for n = 1:1:n_shld+1    % Trailing side fin tip (B)
    t_shld(n) = t_fin + 90 - 180*(n-1)/n_shld;
    xtipb(n) = SBx + d_fin*cosd(t_shld(n));
    ytipb(n) = SBy + d_fin*sind(t_shld(n));
    end

    cle = cosd(t_fin+90); % Initialize angles for fin surfaces
```

```
    sle = sind(t_fin+90);
    cte = cosd(t_fin-90);
    ste = sind(t_fin-90);
     for n = 1:1:n_fin
    xfinab(n) = SAx +(SBx-SAx)*(n)/n_fin;   % Fin center coords
    yfinab(n) = SAy +(SBy-SAy)*(n)/n_fin;
    xLE(n) = xfinab(n) + d_fin*cle;         % Leading side
    yLE(n) = yfinab(n) + d_fin*sle;
    xTE(n) = xfinab(n) + d_fin*cte;         % Trailing side
    yTE(n) = yfinab(n) + d_fin*ste;
     end


% Newtonian Drag (straight fin)*****************************************
 Cp = zeros(n_nose,1);  Cp(1) = 2; cdn = 0; t_cp(1) = 90;
for n = 2:1:n_nose                      % Nose
dy(n) = y_nose(n) - y_nose(n-1);
dx(n) = x_nose(n) - x_nose(n-1);
t_cp(n) = 180 - atand(dy(n)/dx(n));
Cp(n) = Cpmax*sind(t_cp(n))*sind(t_cp(n));
cdn = cdn +  Cp(n) * dy(n) / r_fin ;
end
cdt = 2 * cdn * d_fin/r_nose;           % Fin Tips
Cp_fin = 2 * sind(180 - t_fin)^2;         % Fin Body
cdf = Cp_fin * (yLE(n_fin) - yLE(1)) / r_fin ;

Cd_Newt = cdf+cdt+cdn
% ************************************************************************
 x1a = xtipa;    y1a = ytipa;    % Organize & Concat. Surfaces
 x1b = xLE;      y1b = yLE;
 x1c = xtipb;    y1c = ytipb;
 x1d = fliplr(xTE);      y1d = fliplr(yTE);
 x1 = horzcat(x1a,x1b,x1c,x1d);
 y1 = horzcat(y1a,y1b,y1c,y1d);

else  % ********** Rounded Fin Generation ********************************
    Sbx = SBx;      % Trailing Edge Tip Hinge
    Sby = SBy - r_shld;
    for n = 1:1:n_shld
    t_rad(n)= 90 + t_fin - (n-1)*t_fin/n_shld; % Fin spine angle
    xrad(n) = Sbx + r_shld*cosd(t_rad(n));     % Shoulder centerline
    yrad(n) = Sby + r_shld*sind(t_rad(n));
    xfin(n) = xrad(n) + d_fin*cosd(t_rad(n));  % LE Shoulder Surface
    yfin(n) = yrad(n) + d_fin*sind(t_rad(n));  %
    xfinr(n) = xrad(n) + d_fin*cosd(t_rad(n)+180); % TE ""
    yfinr(n) = yrad(n) + d_fin*sind(t_rad(n)+180);
    end
    for n = 1:1:n_shld+1
    t_shld(n) = 180 - 180*(n-1)/n_shld;        % TE side tip
    xtipb(n) = SBx + d_fin*sind(t_shld(n));
    ytipb(n) = SBy + d_fin*cosd(t_shld(n));
    end
    SAy = r_nose + d_gap + d_fin;              % LE shoulder hinge
    SAx = xfin(1) - (yfin(1) - SAy)/tand(t_fin);
    for n = 1:1:n_shld+1
    t_shld(n) = t_fin - 90 - 180*(n-1)/n_shld;
```

```
    xtipa(n) = SAx + d_fin*cosd(t_shld(n));    % LE Tip surface
    ytipa(n) = SAy + d_fin*sind(t_shld(n));
    end
    cle = cosd(t_fin+90);       % Initialize fin surface angles
    sle = sind(t_fin+90);
    cte = cosd(t_fin-90);
    ste = sind(t_fin-90);
 for n = 1:1:n_fin
    xfinab(n) = SAx +(xrad(1)-SAx)*(n)/n_fin;   % Fin centerline
    yfinab(n) = SAy +(yrad(1)-SAy)*(n)/n_fin;
    xLE(n) = xfinab(n) + d_fin*cle;             % Leading edge coords
    yLE(n) = yfinab(n) + d_fin*sle;
    xTE(n) = xfinab(n) + d_fin*cte;             % Trailing edge coords
    yTE(n) = yfinab(n) + d_fin*ste;
 end

 % Newtonian Drag (rounded fin)*****************************************
 Cp = zeros(n_nose,1);  Cp(1) = 2; cdn = 0; t_cp(1) = 90;
for n = 2:1:n_nose                                % Nose
dy(n) = y_nose(n) - y_nose(n-1);
dx(n) = x_nose(n) - x_nose(n-1);
t_cp(n) = 180 - atand(dy(n)/dx(n));
Cp(n) = Cpmax*sind(t_cp(n))*sind(t_cp(n));
cdn = cdn +  Cp(n) * dy(n) / r_fin ;
end
cdt = cdn * d_fin/r_nose;                          % Tip
Cp_fin = 2 * sind(180 - t_fin)^2;
cdf = Cp_fin * (yLE(n_fin) - yLE(1)) / r_fin ;   % Fin Body
Cp = zeros(n_shld,1);  Cp(1) = Cp_fin; cds = 0; t_cp(1) = t_fin;
for n = 2:1:n_shld
dy(n) = yfin(n) - yfin(n-1);
dx(n) = xfin(n) - xfin(n-1);
t_cp(n) = 180 - atand(dy(n)/dx(n));
Cp(n) = Cpmax*sind(t_cp(n))*sind(t_cp(n));
cds = cds + Cp(n) * dy(n) / r_fin ;              % Shoulder
end

Cd_Newt = cdf+cdt+cdn+cds                      % Total Cd
% *********************************************************************
 x1a=xtipb;             y1a= ytipb;             % Organize & concat
 x1b =fliplr(xfin);     y1b= fliplr(yfin);      % all fin surfaces
 x1c=fliplr(xLE);       y1c= fliplr(yLE);
 x1d =fliplr(xtipa);    y1d= fliplr(ytipa);
 x1e =xTE;              y1e= yTE;
 x1f=xfinr;             y1f= yfinr;
 x1 = horzcat(x1a,x1b,x1c,x1d,x1e,x1f);
 y1 = horzcat(y1a,y1b,y1c,y1d,y1e,y1f);
 x1 = x1 - offset;
end
% *********************************************************************
x=horzcat(x_nose,x_body,x_aft);
y=horzcat(y_nose,y_body,y_aft);
plot(x,y,x1,y1)             % Plot Results
axis([0 1.5*l_body 0 1.5*r_fin])

zlength = length(vertcat(x',x1'));
```

```
z = zeros(zlength,1);
data = [vertcat(x',x1') vertcat(y',y1') z];
a = length(data');
b = 1;
fileID = fopen('TDRVlin.lin','w');
fprintf(fileID, '%6u %6u\r\n',a,b);
fprintf(fileID, '%6.5f %6.5f %6.5f\r\n', data');
fclose(fileID);

zlength = length(x');
z = zeros(zlength,1);
data = [x',y',z];
a = length(data');
b = 1;
fileID = fopen('TDRVlinA.lin','w');
fprintf(fileID, '%6u %6u\r\n',a,b);
fprintf(fileID, '%6.5f %6.5f %6.5f\r\n', data');
fclose(fileID);

zlength = length(x1');
z = zeros(zlength,1);
data = [x1' y1' z;
        x1(1) y1(1) 0];
a = length(data');
b = 1;
fileID = fopen('TDRVlinB.lin','w');
fprintf(fileID, '%6u %6u\r\n',a,b);
fprintf(fileID, '%6.5f %6.5f %6.5f\r\n', data');
fclose(fileID);
```